Advanced Materials 2015 vol: 27 (33) pp: 4823-4829

DOI: 10.1021/acsami.6b09478

High-mobility Sm-doped Bi_2Se_3 ferromagnetic topological insulators and the robust exchange coupling

Taishi Chen, Wenqing Liu, Fubao Zheng, Xingchen Pan, Gerrit van der Laan, Xuefeng Wang, Qinfang Zhang,* Fengqi Song,* Baigeng Wang, Baolin Wang, Yongbing Xu, Rong Zhang, and Guanghou Wang*

T. S. Chen, Dr. W. Q. Liu, X. C. Pan, Prof. X. F. Wang, Prof. F. Q. Song, Prof. B. G. Wang, Prof. Y. B. Xu, Prof. R. Zhang, Prof. G. H. Wang
Collaborative Innovation Center of Advanced Microstructures
National Laboratory of Solid State Microstructures
Nanjing University
Nanjing 210093, P. R. China
E-mail: xfwang@nju.edu.cn; songfengqi@nju.edu.cn

T. S. Chen, X. C. Pan, Prof. F. Q. Song, Prof. B. G. Wang, Prof. G. H. Wang
Department of Physics
Nanjing University
Nanjing 210093, P. R. China

Dr. W. Q. Liu, Prof. X. F. Wang, Prof. Y. B. Xu, Prof. R. Zhang
School of Electronic Science and Engineering
Nanjing University
Nanjing 210093, P. R. China

Dr. W. Q. Liu, Prof. Y. B. Xu
Department of Electronics
University of York
York YO10 5DD, United Kingdom

F. B. Zheng, Prof. Q. F. Zhang, Prof. B. L. Wang
Key Laboratory for Advanced Technology in Environmental Protection of Jiangsu Province
Yancheng Institute of Technology
Yancheng 224051, P. R. China
E-mail: qfangzhang@gmail.com

Prof. G. van der Laan
Diamond Light Source
Didcot OX11 0DE, United Kingdo

KEYWORDS: topological insulators; magnetic doping; XMCD; origin of ferromagnetism

Magnetically-doped topological insulators (MTIs) are emerging as a new platform of dilute magnetic semiconductors (DMSs) due to the potential interest in topological magnetoelectric effect, quantum spin/anomalous Hall effect and Dirac-fermion mediated magnetic coupling physics.[1-12] Intense efforts have been made on intentional magnetic doping of Bi_2Se_3 since the discovery of three dimensional topological insulators (TIs), for which great progress has been made.[12-21] For example, Cr atoms are introduced to Bi_2Se_3 films by molecular beam epitaxy (MBE) growth, which splits the topological Dirac cone and modulates the spin-triplet transport of the anomalous surface electrons.[14, 22] Such modulation leads to the transition from weak antilocalization to weak localization in $(Cr_xBi_{1-x})_2Se_3$ (x = 0.02-0.115) films,[23] where a ferromagnetic coupling is established. Ferromagnetism is also achieved in $(Bi,Cr)_2(Sb,Te)_3$ films, where robust ferromagnetism is found even though there are no residual carriers.[13] Based on the material advance, the quantum anomalous Hall effect has been discovered in MBE-grown $Cr_{0.15}(Bi_{0.1}Sb_{0.9})_{1.85}Te_3$ ultrathin films,[13] where a quantized Hall plateau of $2e^2/h$ is observed without any external fields.[10, 24] Very recently, Chang et al. have further discovered the robust quantum anomalous Hall state in V-doped $(Bi,Sb)_2Te_3$ films,[25] which makes MTIs promising candidates for dissipationless electronic applications.

However, further MTI advance is hindered by the insufficient material quality, which is featured by the low mobility of the samples (typically 10~700 $cm^2V^{-1}s^{-1}$). Although the low mobility suppresses some bulk conduction and may benefit TSS enhancement, the enriched disorders often contribute to some impurity bands in the TIs' bandgap.[26] Such impurity bands are very difficult to eliminate and easy to appear in TIs because of their large dielectric constant and Bohr radius.[27] Such a quality limit may be due to the fact that the recent MTIs are produced by introducing transition metal (TM) dopants including Cr, V, Fe, and Mn.[13, 19, 21, 22, 25, 28] These atoms are expected to substitute the Bi atoms while their atomic sizes are much smaller than Bi, which leads to versatile defects. In some extreme cases, the TM doping is able to suppress the strength of the spin-orbit coupling (SOC) and damages the topological protection of the TI materials.[29]

Rare earth atoms have often large atomic magnetic moments and their atomic size is comparable to Bi. Their SOC is intrinsically strong. The magnetic doping by rare earth atoms sheds light on a high-mobility MTI, which may accommodate more exotic topological physics.[30, 31] Some pioneering attempts on Gd-doped Bi_2Se_3 failed with the result of a paramagnetic phase, probably due to the low doping concentration of only 1 at.%.[18] In this Communication we report the successful preparation of Sm-doped Bi_2Se_3, which exhibits ferromagnetism up to about 52 K and a suppressed bulk electron carrier density of as low as 10^{18} cm^{-3} in order. We observe clear Shubnikov-de Haas (SdH) oscillations in the samples. All these evidences suggest that Sm-doped Bi_2Se_3 is a high-mobility candidate of MTIs.

We prepared the $(Sm_xBi_{1-x})_2Se_3$ crystals with different doping concentrations of $x = 0$, 0.002, 0.005, 0.025, and 0.05 (see Experimental Section). Their real compositions were determined by inductively coupled plasma mass spectrometer (ICP-MS) and X-ray fluorescence spectrometer (XRF), respectively, whose results were fairly consistent with each other. Considering the higher accuracy of ICP-MS analysis (within 0.5 wt.%) than that of XRF analysis (about 5 wt.%), we adopt results from ICP-MS measurements. Their crystalline ordering was examined by X-ray powder diffraction (XRD) technique. **Figure 1**a shows the XRD results of the crystals where the excellent crystallinity is demonstrated according to space group No. 166 (JCPDS card No. 82-0358). Raman spectra were collected at different positions of the pristine cleaved Bi_2Se_3 and doped samples, as shown in Figure 1b,[32] also indicating a good crystalline ordering as well as uniformity of the crystals. After etching the crystal surface by Ar^+ laser irradiation for a few minutes, as shown in Figure 1c, X-ray photoelectron spectroscopy (XPS) measurements demonstrate the absence of O 1s peak, excluding the possible oxidized compounds. Meantime, Sm 4p peaks begin to emerge with the dominant decay of C 1s peak. It is worth noting that the Sm 3d core-level XPS peaks become discernible with the difference in energy between the Sm $3d_{5/2}$ and $3d_{3/2}$ peaks of about 26.8 eV, suggesting that the valence state of Sm dopant is 3+ in the Bi_2Se_3. This rules out a sizeable formation of Sm metallic clusters, indicating the successful preparation of Sm-doped Bi_2Se_3 samples.

Figure 2a shows the field-dependent magnetization curves of a series of samples ($0 \le x \le 0.05$) before subtraction of the diamagnetic background from the sample holder. The crystals show a well-defined hysteresis loops at 10 K when $x \ge 0.025$, while the very lightly doped sample ($x = 0.001$) only hosts a diamagnetic background, probably due to its small paramagnetic signal. Note that undoped Bi_2Se_3 sample ($x = 0$) also exhibits diamagnetic signal, ruling out the possible magnetic contribution from the surface contamination. Figure 2b shows the field-cooled (FC) and zero-field cooled (ZFC) curves of the sample ($x = 0.05$), which coincides above 50 K. The Curie temperature of the sample is deduced to be about 52 K by differentiating first-order magnetization versus temperature from FC curve. An observable feature at 52 K in ZFC curve is merely attributed to the magnetic transition in oxygen adsorbed on the surface of sample during cooling. Its coercive field can reach 500 Oe when $x = 0.05$. The inset in Figure 2a gives the Sm concentration dependence of the coercive field, which increases from nearly zero and clearly starts to rise at $x \ge 0.005$. This agrees with the previous observation of Gd-doped Bi_2Se_3 thin films, in which only a paramagnetic behavior is observed for $x = 0.01$.[18] Further measurements also demonstrate the anisotropic magnetism of the cleaved samples, as shown in Figure 2c with the typical results for $x = 0.025$ sample, where the in-plane coercive field is larger than the out-of-plane coercive field. Note that the different textures of samples do not affect their corresponding anisotropic magnetism. These observations confirm that the observed ferromagnetism is not due to the isotropic clusters such as Sm or Fe clusters; instead it originates from the doped crystals.

The ferromagnetic behavior for the doped samples is correlated with the Sm dopant. This is examined by performing X-ray magnetic circular dichroism (XMCD)[33, 34] measurements. The synchrotron-based X-ray absorption spectroscopy (XAS)/XMCD technique is an ideal valence-, site-, and symmetry-specific probe.[35] Although it has been intensively utilized in the determination of the impurity magnetism of DMSs, its application to TM-doped TIs emerged only very recently.[36] **Figure 3**a presents the typical calculated and experimental XAS and XMCD spectra of the Sm-doped Bi_2Se_3 sample (x = 0.05) recorded at 5 K, which are freshly cleaved immediately before loading into the vacuum chamber. The detailed line shape of the experimental XAS fits the multiplet calculated Sm^{3+}, confirming the trivalent nature of the Sm dopant and pointing to the substitution of Sm in the Bi sites. Small but discernible XMCD, characteristic for a net magnetic moment of Sm, is obtained and shows good agreement with atomic multiplet calculations (Figure 3a).[37] Its line shape features are well reproduced at temperatures up to 50 K, as shown in Figure 3b, dispite the decreasing signal with increasing temperature. The XMCD peak asymmetry at the Sm M_5 edge, i.e., $(\mu^- - \mu^+)/(\mu^- + \mu^+)$, is proportional to the magnetic moment and is plotted versus temperature in the inset of Figure 3b. We observe the same magnitude of the XMCD within error bars for a magnetic field of 3 T and 10 T, indicating a negligible paramagnetic contribution, with the sample magnetism saturating below 3 T. Combining the abovementioned XRD, XPS, superconducting quantum interference device (SQUID) magnetometry and XMCD results, our experiments unambiguously demonstrate an intrinsic Sm-dopant induced ferromagnetism in the sample (x = 0.05) with a Curie temperature of 52 K and a coercive field as high as 500 Oe.

We optimize the material properties by further checking its influence on the Curie temperature. The observed SdH oscillations clearly reveal a high crystalline quality of our samples, as shown in **Figure 4**a. Figure 4b shows the curves for a series of samples with compositional control of Sm and Te. Intentional introduction of Te atoms may introduce some *n*-type carriers. Such control experiments may tune the carrier concentration and the Fermi vector of the materials, which can be critical in the Ruderman-Kittel-Kasuya-Yosida mechanism. We extracted the Fermi vector from the SdH oscillations and the carrier concentrations from the Hall effect measurements, which are plotted against the Curie temperature in Figure 4c and 4d, respectively. Surprisingly, we find that the Curie temperatures remain unchanged under variation of the carrier concentration and Fermi vector by more than one order. This reveals a robust ferromagnetism that is insensitive to carrier concentration.

The supercell structure modelled by density functional theory is shown in **Figure 5**a and the calculated lattice constants ($a = b$ = 8.276 Å, c = 28.64 Å) are consistent with previous results.[38, 39] We firstly consider a single Bi atom substituted by a Sm atom. Such a dopant concentration is 4.17 at.%, comparable to the composition of $(Sm_{0.05}Bi_{0.95})_2Se_3$. Since the ionic radius of Sm^{3+} is closer to that of Bi^{3+} than that of Cr^{3+}, the calculated bond lengths between Bi atoms (4.138 Å) are comparable to the Bi-Sm bond lengths (4.146 Å). This confirms our hypothesis that less defects are present for rare earth

doping. Figure 5b shows the spin-polarized band structure of $SmBi_{23}Se_{36}$, which presents a clear metallic behavior with the energy bands crossing the Fermi level (E_F). It is obvious that the substituted Sm^{3+} ion ($4f^5$ electron configuration) has lost three electrons since there are two unoccupied localized spin-up bands in the vicinity of E_F and five impurity bands below E_F. In $SmBi_{23}Se_{36}$ system, the magnetic moment of the Sm is large, while the other atoms have much smaller magnetic moments (~0.001-0.01 μ_B/atom) aligning antiparallel to that of Sm. Metal-insulator transition occurs when the Sm atom incorporates into the pristine Bi_2Se_3 system. The total and partial density of states (PDOS) of $SmBi_{23}Se_{36}$ are shown in Figure 5c. The almost degenerate DOSs for spin majority and minority are observed from the PDOS of the Bi atom, whereas there is a large spin splitting near E_F for the Sm-4*f* bands. The spin-majority state is partially filled, and the spin-minority state is fully unoccupied, resulting in a total magnetic moment for Sm with a high spin state. This agrees well with the XMCD measurements. Comparing the formation energy of the ferromagnetic and antiferromagnetic configurations we find an energy difference of around a few tens of Kelvin. The calculation confirms the intrinsic ferromagnetic coupling due to the dilutely doped Sm ions.

Our material with robust ferromagnetism appears to be an ideal candidate for a high-mobility MTI. **Table 1** shows the transport parameters of 7 typical samples. We checked the carrier concentration of the samples by Hall measurement, which reaches at least 10^{18} cm^{-3}. It is satisfactory for MTI usage because the crystalline quality is very good, giving very large flakes with a thickness of less than 10 nm. At the optimal thickness of 5-7 nm, this gives an areal density of 10^{12} cm^{-2}, which falls within the working range of SiO_2 or $SrTiO_3$ back gates.[27] The Hall mobility can reach over 10,000 $cm^2V^{-1}s^{-1}$ in some doped samples, which is also confirmed by the observation of the SdH oscillations, as shown in Figure 4a. The delta resistance oscillation is periodic against 1/B, a typical feature of the SdH oscillations. The pronounced SdH oscillation appears at 6-9 T with some Berry phases closer to 0 rather than 0.5, which supports the high mobility of the doped samples. Such high-mobility MTI samples may be promising for quantum Hall studies.

In summary, we have successfully prepared a new type of DMS-based MTI $(Sm_xBi_{1-x})_2Se_3$. It shows an anisotropic ferromagnetic phase for $x = 0.05$, which exhibits a Curie temperature of about 52 K and a typical coercive field of 500 Oe. XMCD analysis shows the polarized spins originate from the Sm dopant atoms. Our evidences point to a robust ferromagnetic coupling, as further supported by first-principles calculations. The higher Curie temperature, the limited carrier density and satisfactory mobility conclusively suggest that it is a high-mobility candidate of MTIs, which acts as an ideal platform for the robust topological edge transport and magnetoelectric effect.

Experimental Section

Sample preparation. Similar to our previous report,[40] the $(Sm_xBi_{1-x})_2Se_3$ samples with $x = 0$, 0.002, 0.005, 0.025, and 0.05 were prepared by the melting method, during which mixed high-purity Bi, Se and Sm powders (99.999% purity, Alfa Aesar, in a designed molar ratio) were sealed in clean silica ampoules. The mixtures were then heated to 950ºC in one day and kept at this temperature for five days, while slowly stirred at a speed of 5 turns/minute. After cooling slowly down to 550ºC over fifteen days, the materials were annealed at 550ºC for five days before cooling down to room temperature. The obtained crystals were then cleaved with a razor blade, resulting in large crystalline flakes with a thickness ranging from 1 to 500 μm and lateral dimensions of a few mm.

Characterization. The chemical compositions were determined by ICP-MS (Perkin Elmer Optima 5300DV) and the XRF (ARL 9800), respectively. The XRD measurements were carried out on a CAD4/PC (Enraf Nonius) diffractometer and on an X'Pert PRO (Philips) diffractometer. Raman spectra were acquired from a micro-Raman spectrometer (NT-MDT nanofinder-30) with a 514.5 nm Ar^+ laser as the excitation source in a backscattering geometry. The laser spot size on samples was 1-2 mm in diameter, and the incident laser power was below 1 mW without damaging the studied samples. Sm 4p, Sm 3d and O 1s core-level spectra were measured by XPS (UlVAC-PHI 5000 VersaProbe) using a Al Ka source in an ultrahigh-vacuum chamber. The peak positions were referenced to the adventitious C 1s peak at 284.5 eV. The surface band-bending effect as well as atmospherc contamination could be eliminated by Ar^+ laser irradiation during XPS measurements. Magnetic properties were measured by a SQUID magnetometer (Quantum Design MPMS XL-7). XAS and XMCD measurements at the Sm $M_{5,4}$ absorption edges were performed on Beamline I10 at Diamond Light Source, United Kingdom. X-rays with c.a. 100% degree of circular polarization were used in normal incidence with respect to the sample plane and parallel to the applied magnetic field (i.e., Faraday geometry). XAS experiments were carried out at various temperatures from 3 to 50 K using total florescence yield (TFY) detection. The XMCD was obtained by taking the difference of the XAS spectra, i.e., $m^- - m^+$, by flipping the X-ray helicity at fixed magnetic field of 3 T, under which the sample is fully magnetized with little paramagnetic contribution. For the electrical transport measurements, six probe electrodes were mounted onto the cleaved samples using room temperature cured silver paste (see a typical photograph in the inset of Figure 4a). The transport properties were measured in a Quantum Design Physical Property Measurement System (PPMS; 9 T) and a home-made measurement system.

First-principles calculations. To investigate the electronic and magnetic properties of bulk Bi_2Se_3 with dilute Sm doping, a 2×2×1 supercell containing 24 Bi and 36 Se atoms is employed for spin-polarized density functional theory (DFT) with an all-electron linearized augmented plane wave (FLAPW) method embedded in the WIEN2K code.[41] A generalized gradient approximation (GGA)[42] is used to treat the electron exchange and correlation. The muffin-tin radii are chosen as 2.5 a.u. for Bi,

Se and Sm atoms. The parameter $R_{min}K_{max}$, which controls the size of the basis set in our calculations, is chosen as 6.0. The Brillouin zone (BZ) is represented by a set of 6×6×2 *k*-points[43] for the geometry optimizations and for the static total energy calculations. All atoms in the supercell were allowed to relax freely until the maximum Hellmann-Feynman force is smaller than 0.01 eV $Å^{-1}$. Note that the appropriate SOC strength is also optimized by fitting the experimental bandgap of 0.3 eV for the pristine Bi_2Se_3.

Acknowledgements

T. S. Chen, W. Q. Liu, and F. B. Zheng contributed equally to this work. This work is supported by National Key Projects for Basic Research of China (Nos. 2014CB921103 and 2013CB922103), National Natural Science Foundation of China (Nos. 61176088, 11274003, 91421109, 61229401, 11474246, and 11204265), the New Century Excellent Talents Program in University (No. NCET-11-0240), the PAPD project, the Qing Lan project, the Natural Science Foundation of Jiangsu Province (Nos. BK20130054 and BK2013118), the Program A Scheme for Outstanding PhD candidate of Nanjing University, and the Fundamental Research Funds for the Central Universities. We would like to acknowledge the helpful assistance of the Nanofabrication and Characterization Center at the Physics College of Nanjing University. Helpful assistance from Dr. L. Pi and Prof. Y. H. Zhang at High Magnetic Field Laboratory of CAS is also acknowledged.

References

[1] J. H. Bardarson, J. E. Moore, *Rep. Prog. Phys.* **2013**, *76*, 056501.

[2] M. Z. Hasan, C. L. Kane, *Rev. Mod. Phys.* **2010**, *82*, 3045.

[3] J. Chen, X. Y. He, K. H. Wu, Z. Q. Ji, L. Lu, J. R. Shi, J. H. Smet, Y. Q. Li, *Phys. Rev. B* **2011**, *83*, 241304(R).

[4] W. K. Tse, A. H. MacDonald, *Phys. Rev. B* **2010**, *82*, 161104.

[5] B. A. Bernevig, T. L. Hughes, S. C. Zhang, *Science* **2006**, *314*, 1757.

[6] Y. L. Chen, J. H. Chu, J. G. Analytis, Z. K. Liu, K. Igarashi, H. H. Kuo, X. L. Qi, S. K. Mo, R. G. Moore, D. H. Lu, M. Hashimoto, T. Sasagawa, S. C. Zhang, I. R. Fisher, Z. Hussain, Z. X. Shen, *Science* **2010**, *329*, 659.

[7] D. Hsieh, Y. Xia, L. Wray, D. Qian, A. Pal, J. H. Dil, J. Osterwalder, F. Meier, G. Bihlmayer, C. L. Kane, Y. S. Hor, R. J. Cava, M. Z. Hasan, *Science* **2009**, *323*, 919.

[8] R. Yu, W. Zhang, H. J. Zhang, S. C. Zhang, X. Dai, Z. Fang, *Science* **2010**, *329*, 61.

[9] X. F. Kou, S. T. Guo, Y. B. Fan, L. Pan, M. R. Lang, Y. Jiang, Q. M. Shao, T. X. Nie, K. Murata, J. S. Tang, Y. Wang, L. He, T. K. Lee, W. L. Lee, K. L. Wang, *Phys. Rev. Lett.* **2014**, *113*, 137201.

[10] J. G. Checkelsky, R. Yoshimi, A. Tsukazaki, K. S. Takahashi, Y. Kozuka, J. Falson, M. Kawasaki, Y. Tokura, *Nat. Phys.* **2014**, *10*, 731.

[11] K. Nomura, N. Nagaosa, *Phys. Rev. Lett.* **2011**, *106*, 166802.

[12] C. Z. Chang, J. S. Zhang, M. H. Liu, Z. C. Zhang, X. Feng, K. Li, L. L. Wang, X. Chen, X. Dai, Z. Fang, X. L. Qi, S. C. Zhang, Y. Y. Wang, K. He, X. C. Ma, Q. K. Xue, *Adv. Mater.* **2013**, *25*, 1065.

[13] C. Z. Chang, J. S. Zhang, X. Feng, J. Shen, Z. C. Zhang, M. H. Guo, K. Li, Y. B. Ou, P. Wei, L. L. Wang, Z. Q. Ji, Y. Feng, S. H. Ji, X. Chen, J. F. Jia, X. Dai, Z. Fang, S. C. Zhang, K. He, Y. Y. Wang, L. Lu, X. C. Ma, Q. K. Xue, *Science* **2013**, *340*, 167.

[14] Q. I. Yang, M. Dolev, L. Zhang, J. F. Zhao, A. D. Fried, E. Schemm, M. Liu, A. Palevski, A. F. Marshall, S. H. Risbud, A. Kapitulnik, *Phys. Rev. B* **2013**, *88*, 081407.

[15] X. F. Kou, M. R. Lang, Y. B. Fan, Y. Jiang, T. X. Nie, J. M. Zhang, W. J. Jiang, Y. Wang, Y.

G. Yao, L. He, K. L. Wang, *ACS Nano* **2013**, *7*, 9205.

[16] P. P. J. Haazen, J. B. Laloe, T. J. Nummy, H. J. M. Swagten, P. Jarillo-Herrero, D. Heiman, J. S. Moodera, *Appl. Phys. Lett.* **2012**, *100*, 082404.

[17] T. C. Hsiung, D. Y. Chen, L. Zhao, Y. H. Lin, C. Y. Mou, T. K. Lee, M. K. Wu, Y. Y. Chen, *Appl. Phys. Lett.* **2013**, *103*, 163111.

[18] Y. R. Song, F. Yang, M. Y. Yao, F. F. Zhu, L. Miao, J. P. Xu, M. X. Wang, H. Li, X. Yao, F. H. Ji, S. Qiao, Z. Sun, G. B. Zhang, B. Gao, C. H. Liu, D. Qian, C. L. Gao, J. F. Jia, *Appl. Phys. Lett.* **2012**, *100*, 242403.

[19] J. J. Cha, M. Claassen, D. S. Kong, S. S. Hong, K. J. Koski, X. L. Qi, Y. Cui, *Nano Lett.* **2012**, *12*, 4355.

[20] L. R. Shelford, T. Hesjedal, L. Collins-McIntyre, S. S. Dhesi, F. Maccherozzi, G. van der Laan, *Phys. Rev. B* **2012**, *86*, 081304.

[21] H. J. Kim, K. S. Kim, J. F. Wang, V. A. Kulbachinskii, K. Ogawa, M. Sasaki, A. Ohnishi, M. Kitaura, Y. Y. Wu, L. Li, I. Yamamoto, J. Azuma, M. Kamada, V. Dobrosavljevic, *Phys. Rev. Lett.* **2013**, *110*, 136601.

[22] C. Z. Chang, P. Z. Tang, Y. L. Wang, X. Feng, K. Li, Z. C. Zhang, Y. Y. Wang, L. L. Wang, X. Chen, C. X. Liu, W. H. Duan, K. He, X. C. Ma, Q. K. Xue, *Phys. Rev. Lett.* **2014**, *112*, 056801.

[23] M. H. Liu, J. S. Zhang, C. Z. Chang, Z. C. Zhang, X. Feng, K. Li, K. He, L. L. Wang, X. Chen, X. Dai, Z. Fang, Q. K. Xue, X. C. Ma, Y. Y. Wang, *Phys. Rev. Lett.* **2012**, *108*, 036805.

[24] X. F. Kou, S. Guo, Y. Fan, L. Pan, M. R. Lang, Y. Jiang, Q. Shao, T. Nie, K. Murata, J. Tang, Y. Wang, L. He, T. Lee, W. Lee, K. L. Wang, *Phys. Rev. Lett.* **2014**, *113*, 137201.

[25] C. Z. Chang, W. W. Zhao, D. Y. Kim, H. J. Zhang, B. A. Assaf, D. Heiman, S. C. Zhang, C. X. Liu, M. H. W. Chan, J. S. Moodera, *Nat. Mater.* **2015**, *14*, 473.

[26] Z. Ren, A. A. Taskin, S. Sasaki, K. Segawa, Y. Ando, *Phys. Rev. B* **2010**, *82*, 241306.

[27] G. Zhang, H. J. Qin, J. Chen, X. Y. He, L. Lu, Y. Q. Li, K. H. Wu, *Adv. Funct. Mater.* **2011**, *21*, 2351.

[28] M. R. Scholz, J. Sanchez-Barriga, D. Marchenko, A. Varykhalov, A. Volykhov, L. V. Yashina, O. Rader, *Phys. Rev. Lett.* **2012**, *108*, 256810.

[29] J. S. Zhang, C. Z. Chang, P. Z. Tang, Z. C. Zhang, X. Feng, K. Li, L. L. Wang, X. Chen, C. X.

Liu, W. H. Duan, K. He, Q. K. Xue, X. C. Ma, Y. Y. Wang, *Science* **2013**, *339*, 1582.

[30] Y. Yan, L. X. Wang, X. X. Ke, G. Van Tendeloo, X. S. Wu, D. P. Yu, Z. M. Liao, *Sci. Rep.* **2014**, *4*, 3817.

[31] D. X. Qu, Y. S. Hor, J. Xiong, R. J. Cava, N. P. Ong, *Science* **2010**, *329*, 821.

[32] G. H. Zhang, H. J. Qin, J. Teng, J. D. Guo, Q. L. Guo, X. Dai, Z. Fang, K. H. Wu, *Appl. Phys. Lett.* **2009**, *95*, 053114.

[33] G. van der Laan, B. T. Thole, *Phys. Rev. B* **1991**, *43*, 13401.

[34] G. van der Laan, A.I. Figueroa, *Coord. Chem. Rev.* **2014**, *277-278*, 95.

[35] W. Q. Liu, Y. B. Xu, P. K. J. Wong, N. J. Maltby, S. P. Li, X. F. Wang, J. Du, B. You, J. Wu, P. Bencok, R. Zhang, *Appl. Phys. Lett.* **2014**, *104*, 142407.

[36] W. Q. Liu, L. He, Y. B. Xu, K. Murata, M. C. Onbasli, M. Lang, N. J. Maltby, S. P. Li, X. F. Wang, C. A. Ross, P. Bencok, G. van der Laan, R. Zhang, K. L. Wang, *Nano Lett.* **2015**, *15*, 764.

[37] B. T. Thole, G. van der Laan, J. C. Fuggle, G. A. Sawatzky, R. C. Karnatak, J. M. Esteva, *Phys. Rev. B* **1985**, *32*, 5107.

[38] M. I. Zargarova, P. K. Babaeva, D. S. Azhdarova, Z. D. Melikova, S. A. Mekhtieva, *Inorg. Mater.* **1995**, *31*, 2.

[39] H. J. Zhang, C. X. Liu, X. L. Qi, X. Dai, Z. Fang, S. C. Zhang, *Nat. Phys.* **2009**, *5*, 438.

[40] T. S. Chen, Q. Chen, K. Schouteden, W. K. Huang, X. F. Wang, Z. Li, F. Miao, X. R. Wang, Z. G. Li, B. Zhao, S. C. Li, F. Q. Song, J. L. Wang, B. G. Wang, C. Van Haesendonck, G. H. Wang, *Nat. Commun.* **2014**, *5*, 5022.

[41] K. Schwarz, P. Blaha, *Comput. Mater. Sci.* **2003**, *28*, 259.

[42] J. P. Perdew, K. Burke, M. Ernzerhof, *Phys. Rev. Lett.* **1997**, *78*, 1396.

[43] L. H. Ye, A. J. Freeman, B. Delley, *Phys. Rev. B* **2006**, *73*, 033203.

References

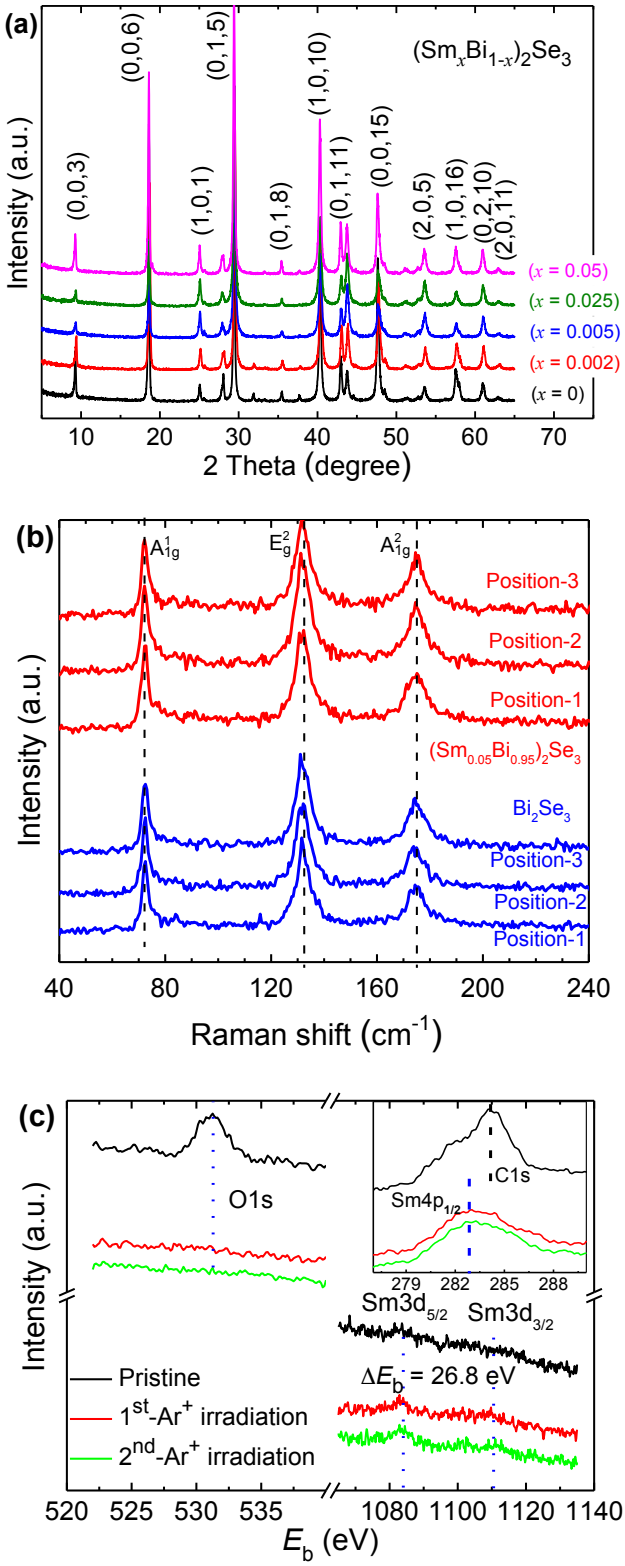

Figure 1. Structural analyses of the Sm-doped Bi_2Se_3 crystals. a) Powder XRD patterns of all $(Sm_xBi_{1-x})_2Se_3$ samples. b) Raman spectra of Bi_2Se_3 and $(Sm_{0.05}Bi_{0.95})_2Se_3$ at different positions. c) High-resolution XPS spectra of Sm 4p, Sm 3d and O 1s peaks without and with 1st and 2nd round Ar^+ laser irradiation for the $(Sm_{0.05}Bi_{0.95})_2Se_3$ sample.

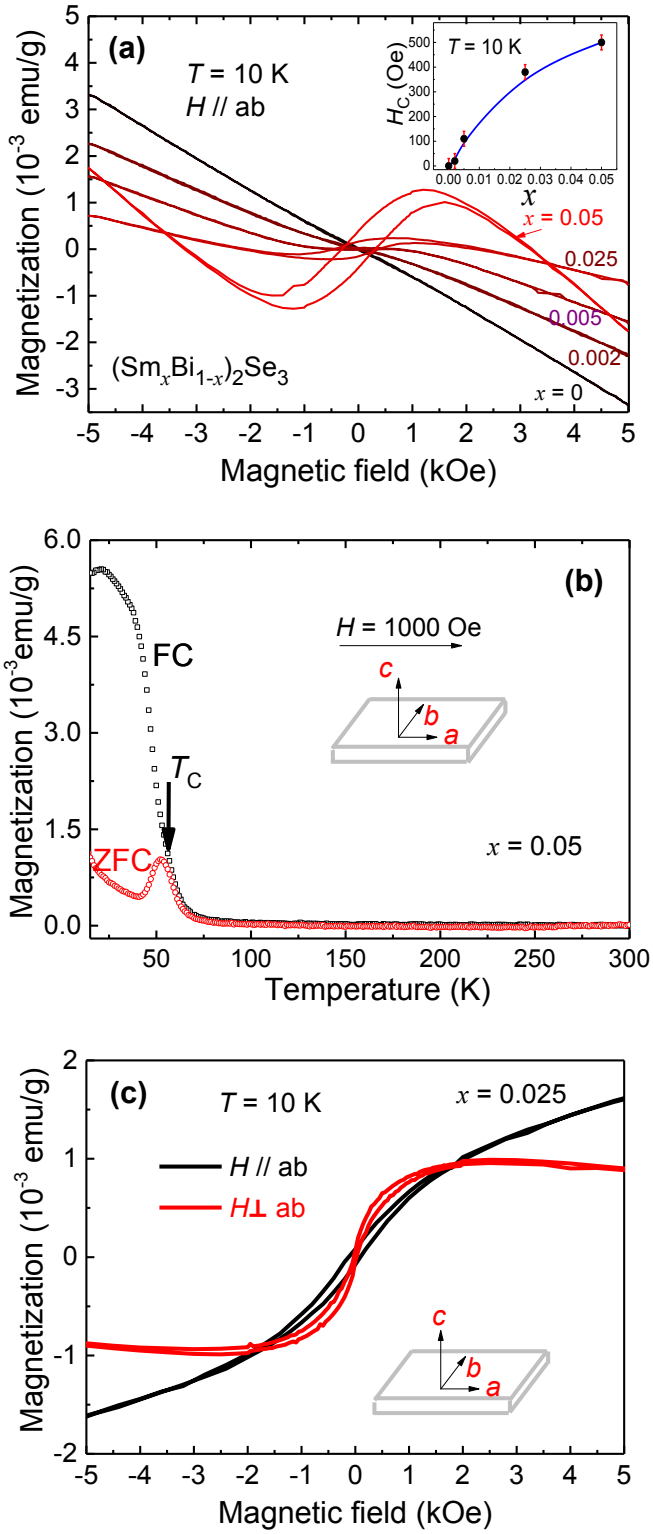

Figure 2. Magnetic characterization of the perfect crystals of $(Sm_xBi_{1-x})_2Se_3$. a) Raw data of the magnetization measurements at 10 K for all the $(Sm_xBi_{1-x})_2Se_3$ samples without subtraction of diamagnetic signals. The increased coercive field with increasing Sm concentration (x) is shown in the inset. b) ZFC-FC curves of $(Sm_{0.05}Bi_{0.95})_2Se_3$ with fixed magnetic field (1000 Oe) parallel to ab plane. c) In-plane and out-of-plane magnetic hysteresis loops at 10 K for $(Sm_{0.025}Bi_{0.975})_2Se_3$, which confirms the in-plane easy axis.

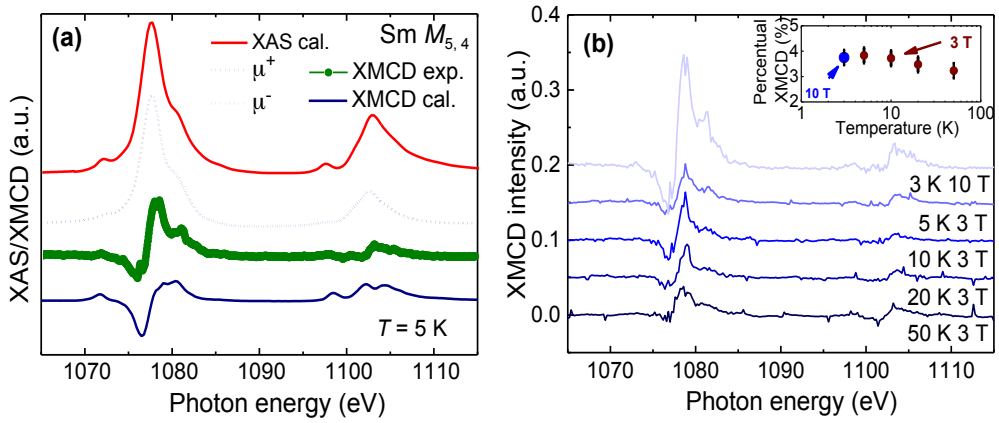

Figure 3. XAS and XMCD spectra of freshly cleaved $(Sm_{0.05}Bi_{0.95})_2Se_3$. a) Typical pair of XAS and XMCD spectra obtained at 5 K with TFY detection in comparison with atomic multiplet calculations. Data are offset and the XMCD intensity is 10× enlarged for clarity. b) Typical XMCD spectra obtained at temperatures from 5 to 50 K at 3 T. Spectra have been offset for clarity. The inset shows the percentual XMCD at the Sm M_5 edge against temperature. The data for 3 K was recorded at a magnetic field of 10 T while the rest was recorded at 3 T. Note the horizontal axis has a logarithmic scale.

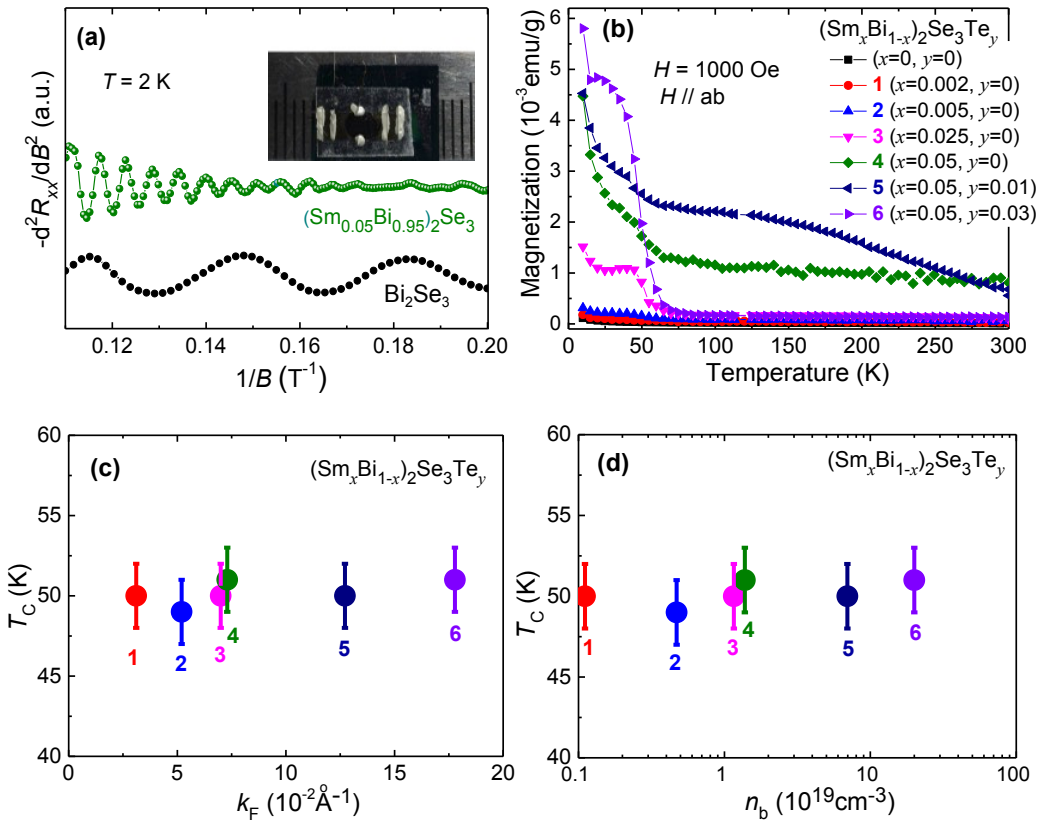

Figure 4. Control experiment for addressing the origin of magnetism in $(Sm_xBi_{1-x})_2Se_3$ by introducing a fraction of Te atoms. a) SdH oscillations in Bi_2Se_3 and $(Sm_{0.05}Bi_{0.95})_2Se_3$ crystals at 2 K, revealing the excellent crystalline quality. Fermi wave vectors and carrier concentration can be deduced. The inset shows the typical photograph for a Hall bar device, where six ohmic contacts are made with room temperature cured silver paste. b) Summary of FC data of all $(Sm_xBi_{1-x})_2Se_3Te_y$ samples under a field of 1000 Oe. c) Relationship between Curie temperature (T_c) and Fermi wave vector (k_F). d) Relationship between T_c and carrier concentration (n_b), indicating a carrier-independent magnetism.

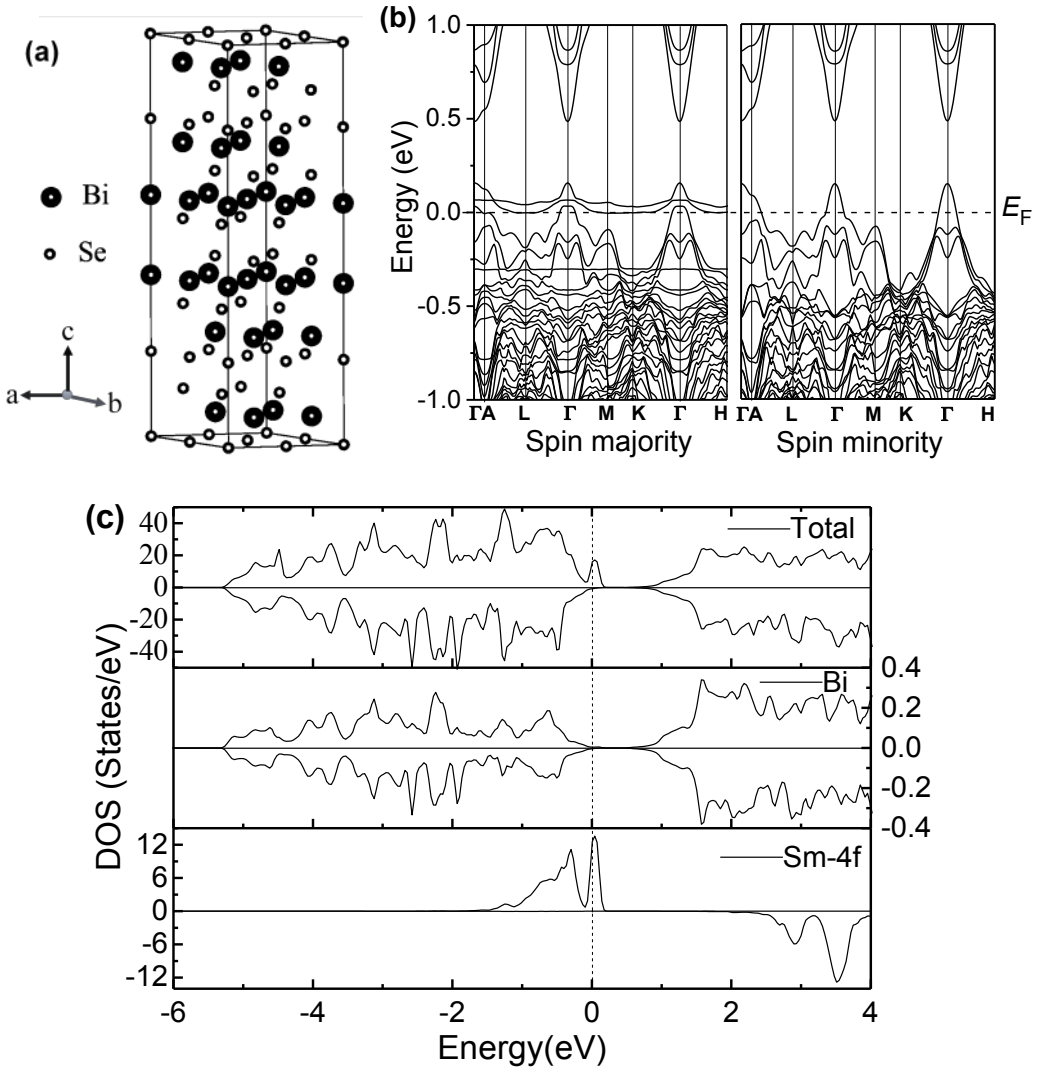

Figure 5. Modeling the magnetic coupling in Sm-doped Bi_2Se_3. a) Supercell structure of 2×2×1 of Bi_2Se_3. b) Spin-polarized electronic band structures. c) DOS of $SmBi_{23}Se_{36}$ and PDOSs for Bi atom and Sm with 4f electron configuration. The Fermi level is plotted with the dotted line.

Table

Sample $(Sm_xBi_{1-x})_2Se_3Te_y$ (x, y)	Resistivity (mΩ·cm) at 2 K	Mobility ($cm^2V^{-1}s^{-1}$) at 2 K	Carrier density (cm^{-3}) at 2 K	Fermi vector ($Å^{-1}$) at 2 K	Coercive field (Oe) at 10 K	Curie Temperature (K)
(0, 0)	0.35	18000	1.0×10^{18}	0.020	0	-
(0.002, 0)	0.51	12000	1.2×10^{18}	0.025	15	50
(0.005, 0)	0.12	10500	5.0×10^{18}	0.050	112	48
(0.025, 0)	0.071	8100	1.1×10^{19}	0.062	380	50
(0.05, 0)	0.063	7200	1.4×10^{19}	0.070	500	52
(0.05, 0.01)	0.041	2200	7.0×10^{19}	0.125	492	50
(0.05, 0.03)	0.022	1500	2.0×10^{20}	0.180	500	51

Table 1. Summary of the typical parameters of all 7 samples (x = 0-0.05; y = 0-0.03).